

Microwave absorption properties regulation and bandwidth formula of oriented $Y_2Fe_{17}N_{3-\delta}$@SiO_2/PU composite synthesized by reduction—diffusion method

Hao Wang(王浩), Liang Qiao(乔亮), Zu-Ying Zheng(郑祖应), Hong-Bo Hao(郝宏波), Tao Wang(王涛), Zheng Yang(杨正), and Fa-Shen Li(李发伸)

Citation: Chin. Phys. B, 2022, 31 (**11**): 114206. DOI: 10.1088/1674-1056/ac81ac

What follows is a list of articles you may be interested in

Dual-function terahertz metasurface based on vanadium dioxide and graphene

Jiu-Sheng Li(李九生)† and Zhe-Wen Li(黎哲文)

Chin. Phys. B, 2022, 31 (**9**): 094201. DOI: 10.1088/1674-1056/ac5884

Dynamically tunable multiband plasmon-induced transparency effect based on graphene nanoribbon waveguide coupled with rectangle cavities system

Zi-Hao Zhu(朱子豪), Bo-Yun Wang(王波云), Xiang Yan(闫香), Yang Liu(刘洋), Qing-Dong Zeng(曾庆栋), Tao Wang(王涛), and Hua-Qing Yu(余华清)

Chin. Phys. B, 2022, 31 (**8**): 084210. DOI: 10.1088/1674-1056/ac7e39

Reflection and transmission of an Airy beam in a dielectric slab

Xiaojin Yang(杨小锦), Tan Qu(屈檀), Zhensen Wu(吴振森), Haiying Li(李海英), Lu Bai(白璐), Lei Gong(巩蕾), and Zhengjun Li(李正军)

Chin. Phys. B, 2022, 31 (**7**): 074202. DOI: 10.1088/1674-1056/ac4e07

Single-polarization single-mode hollow-core negative curvature fiber with nested U-type cladding elements

Qi-Wei Wang(王启伟), Shi Qiu(邱石), Jin-Hui Yuan(苑金辉), Gui-Yao Zhou(周桂耀), Chang-Ming Xia(夏长明), Yu-Wei Qu(屈玉玮), Xian Zhou(周娴), Bin-Bin Yan(颜玢玢), Qiang Wu(吴强), Kui-Ru Wang(王葵如), Xin-Zhu Sang(桑新柱), and Chong-Xiu Yu(余重秀)

Chin. Phys. B, 2022, 31 (**6**): 064213. DOI: 10.1088/1674-1056/ac46c7

On chip chiral and plasmonic hybrid dimer or tetramer: Generic way to reverse longitudinal and lateral optical binding forces

Sudipta Biswas, Roksana Khanam Rumi, Tasnia Rahman Raima, Saikat Chandra Das, and M R C Mahdy

Chin. Phys. B, 2022, 31 (**5**): 054202. DOI: 10.1088/1674-1056/ac322d

---

Microwave absorption properties regulation and bandwidth formula of oriented $Y_2Fe_{17}N_{3-\delta}$@SiO_2/PU composite synthesized by reduction–diffusion method

Hao Wang(王浩)[1], Liang Qiao(乔亮)[1,†], Zu-Ying Zheng(郑祖应)[1], Hong-Bo Hao(郝宏波)[2], Tao Wang(王涛)[1], Zheng Yang(杨正)[1], and Fa-Shen Li(李发伸)[1]

[1] *Institute of Applied Magnetism, Key Laboratory for Magnetism and Magnetic Materials of Ministry of Education, Lanzhou University, Lanzhou* 730000, *China*

[2] *State Key Laboratory of Baiyunobo Rare Earth Resource Researches and Comprehensive Utilization, Baotou* 014000, *China*

(Received 23 May 2022; revised manuscript received 14 July 2022; accepted manuscript online 18 July 2022)

As concepts closely related to microwave absorption properties, impedance matching and phase matching were rarely combined with material parameters to regulate properties and explore related mechanisms. In this work, reduction–diffusion method was innovatively applied to synthesize rare earth alloy Y_2Fe_{17}. In order to regulate the electromagnetic parameters of absorbers, the $Y_2Fe_{17}N_{3-\delta}$ particles were coated with silica ($Y_2Fe_{17}N_{3-\delta}$@SiO_2) and absorbers with different volume fractions were prepared. The relationship between impedance matching, matching thickness, and the strongest reflection loss peak (RL_{min}) was presented obviously. Compared to the microwave absorption properties of $Y_2Fe_{17}N_{3-\delta}$/PU absorber, $Y_2Fe_{17}N_{3-\delta}$@SiO_2/PU absorbers are more conducive to the realization of microwave absorption material standards which are thin thickness, light weight, strong absorbing intensity, and broad bandwidth. Based on microwave frequency bands, the microwave absorption properties of the absorbers were analyzed and the related parameters were listed. As an important parameter related to perfect matching, reflection factor ($\sqrt{\varepsilon_r/\mu_r}$) was discussed combined with microwave amplitude attenuation. According to the origin and mathematical model of bandwidth, the formula of EAB ($RL < -10$ dB) was derived and simplified. The calculated bandwidths agreed well with experimental results.

Keywords: microwave absorption, rare earth alloy, reduction–diffusion method, $Y_2Fe_{17}N_{3-\delta}$@SiO_2, reflection factor, impedance and phase matching, bandwidth formula

PACS: 42.25.Bs, 75.50.Bb, 76.30.Kg, 78.20.Ci **DOI:** 10.1088/1674-1056/ac81ac

1. Introduction

In the present society, as an important carrier of information transmission, microwave is widely used in human life, production, and military equipment. However, owing to the rapid development of high frequency wireless communication technology and the application of various electronic devices, electromagnetic radiation interferes with the operation of electronic equipment and reduces the operation life increasing seriously.[1] In addition, the advancement of radar technology in different frequency bands also brings severe challenges to stealth military equipment. Therefore, the development of high-efficiency microwave absorption materials with properties including light weight, thin thickness, strong absorption strength, wide efficient microwave absorption materials has become an urgent demand.

In the past studies, researchers have tried a variety of materials. These microwave absorption materials can be mainly divided into dielectric-loss-type materials, magnetic materials.[2] Dielectric-loss materials are coal-based carbon,[3] biochar,[4] and conductivity polymers, *etc.*; magnetic materials are ferrites,[2] transition metals,[5] and metal alloy,[6] *etc*. In addition, the microwave absorption properties can be adjusted by changing morphology, size, and distribution of materials, like three-dimensional (3D) biological carbon,[4] layered structure,[6] carbon nanotubes,[7] nanospheres,[8] and hollow core–shell structure,[9] *etc*. The above factors provide various options and ideas for microwave absorption researches.

In the past ten years, as magnetic material which has great potential in microwave absorption, rare earth alloy has been concerned and studied by researchers, microwave absorption properties of which are shown in Table 1. As one of the rare earth alloys, $Y_2Fe_{17}N_{3-\delta}$ have potential in high frequency applications due to strong easy-plane anisotropy.[10] At present, the researches on $Y_2Fe_{17}N_{3-\delta}$ mainly focus on the field of high frequency soft magnetic composites (SMCs) and high frequency wave absorption.[10,11] On the one hand, as a magnetic material with similar property, $Ce_2Fe_{17}N_{3-\delta}$ provides theoretical basis and practical data for high-frequency soft magnetic application of $Y_2Fe_{17}N_{3-\delta}$.[12] On the other hand, the exploration of $Y_2Fe_{17}N_{3-\delta}$'s microwave absorption property is still in the simple characterization stage of calculating reflection losses under given absorber thicknesses.[10] In addition, arc melting and a long homogeneous annealing were used to synthesize rare earth alloys in previous studies, which limits the production and complicates the process.[13,14] Therefore, it is urgent to explore and apply a new synthesis process to produce rare earth alloys efficiently in large quantities.

[†]Corresponding author. E-mail: qiaoliang@lzu.edu.cn

© 2022 Chinese Physical Society and IOP Publishing Ltd

Table 1. Microwave absorption properties of different rare earth alloy composites.

Sample	Loading ratio	Thickness (mm)	f_m (GHz)	EAB (GHz)	RL_{min} (dB)	Ref.
$Ce_2Co_{16.6}Ni_{0.4}$	–	1.60	9.60	3.25	–44.29	[14]
		1.40	11.34	3.36	–41.53	
$Ce_{1.8}Sm_{0.2}Fe_{17}N_{3-\delta}$/paraffin	25 wt%	3.00	3.30	1.0 (RL < −20 dB)	–39.00	[15]
$Dy_{0.3}Pr_{1.7}Fe_{17}$/paraffin	20 wt%	1.80	7.36	1.92	–28.91	[16]
$Ce_2Fe_{17}N_{3-\delta}$/silicone	15 vol%	1.91	9.01	3.67	–61.30	[17]
$Dy_{0.2}Ce_{1.8}Co_{17}$/paraffin	20 wt%	1.80	8.00	2.64	–39.16	[18]
$Pr_{0.2}Ce_{1.8}Co_{17}$/paraffin	20 wt%	2.24	7.92	2.24	–36.80	[18]
$Y_2Fe_{16}Si$/paraffin	25 wt%	1.80	10.51	4.40	–51.60	[19]
	25 wt%	1.90	9.80	4.00	–33.40	
	25 wt%	1.38	14.90	6.00	–29.20	
$Y_2Fe_{17}N_{3-\delta}$/paraffin	30 vol%	2.65	2.45	0.66	–16.60	[10]

As mentioned above, although the researchers have tried many materials and enumerated related data in detail to prove that their synthesized materials have excellent microwave absorption properties. However, these studies simply change the material parameters and calculate reflection losses (RL) by transmission line theory without exploring underlying mechanisms and considering frequency bands of application. As a result, microwave absorption materials have been made little progress in identifying microwave absorption mechanism and the realization of the goal of "thin thickness, light weight, wide bandwidth, strong absorbing intensity".[5] From what has been discussed above, it is urgent to clarify the mechanisms of microwave absorption and unify the evaluation standards of microwave absorbing material in order to promote the research progress of microwave absorption.

In the present work, the $Y_2Fe_{17}N_{3-\delta}$@SiO_2 particles were synthesized by reduction–diffusion method, high pressure nitriding technology, and silica coating method. The structure, morphology, elements, and magnetic properties of $Y_2Fe_{17}N_{3-\delta}$ and $Y_2Fe_{17}N_{3-\delta}$@SiO_2 particles were characterized. The impedance matching and microwave absorption properties of $Y_2Fe_{17}N_{3-\delta}$@SiO_2/PU absorbers were calculated and compared with those of $Y_2Fe_{17}N_{3-\delta}$/PU absorbers. The result indicates that $Y_2Fe_{17}N_{3-\delta}$@SiO_2/PU absorbers are more conducive to the realization of microwave absorption material standards which are thin thickness, light weight, strong absorbing intensity, and broad bandwidth. The reflection factor ($\sqrt{\varepsilon_r/\mu_r}$) is closely related to the perfect matching of absorbers. The formula of EAB is derived and simplified. The bandwidths from the theoretical calculations under various thicknesses are almost in accordance with those of the experimental results.

2. Experiment

2.1. Raw materials and synthesis

The raw materials of synthesizing Y_2Fe_{17} are Y_2O_3 powder (purity 99.99%, 3 μm–5 μm), carbonyl iron powder (spherical, purity 99.9%, 3 μm–5 μm), and calcium (purity 99%, 3 mm). Based on the atomic ratio of Y_2Fe_{17}, an additional 50% of Y_2O_3 powder was added to make up for the volatilization loss of Y in the reduction–diffusion process; On the basis of excess Y_2O_3, an additional 50% of the calcium was added to reduce Y_2O_3 to Y fully. The raw materials were continuously mixed in argon atmosphere using a 3D mixing machine for 9 h. Finally, the mixture was pressed into a cylindrical shape under the pressure of 15 MPa and was moved to a tube furnace. The reduction–diffusion method was carried out in flowing Ar (200 mL/min). First of all, the temperature of the furnace needed to be raised and kept at 800 °C–1100 °C for 13 h. Then, the temperature was naturally cooled to room temperature in the atmosphere of flowing Ar. Finally, the alloy ingots after the reaction was broken to particles with size range at ∼ 50 μm by a jaw crusher.

The broken $Y_2Fe_{17}N_{3-\delta}$ particles reacted reversibly with H_2 to make the particles smaller and then were moved into a high pressure reaction equipment. The high pressure nitriding process needed to be at 480 °C under N_2 (purity 99.9999%) atmosphere of 10 MPa for 4 h. The particles after nitriding were cleaned and filtered with ammonium acetate solution (5 wt%) to remove CaO and excess Ca and then was cleaned with ethanol to remove water. Finally, the $Y_2Fe_{17}N_{3-\delta}$ particles were obtained by drying in vacuum drying oven. The above synthesis process of $Y_2Fe_{17}N_{3-\delta}$ particles and related process parameters were shown in Fig. 1. Then, the $Y_2Fe_{17}N_{3-\delta}$ particles were further broken with the size range at ∼ 5 μm through the planetary ball milling (250 r/min, 4 h) for the follow-up processes.

2.2. Coating process and absorber preparation

In order to change complex permeability and permittivity for regulating impedance matching, the silicon dioxide coating process was employed to synthesize $Y_2Fe_{17}N_{3-\delta}$@SiO_2 particles.[20] In this process, the stirrer kept rotating to ensure that materials were evenly dispersed in the solution. Firstly, 5-g $Y_2Fe_{17}N_{3-\delta}$ (∼ 5 μm) particles were added and dispersed in 150-mL ethanol (99.7 wt%). Secondly, 2-mL 3-aminopropyl

triethoxysilane (98 wt%) was added to the solution as a surfactant and the liquid–air interface became milky white after stirring 10 minutes. Then, 40-mL deionized water, 20-mL ammonia solution (25 wt%–28 wt%), and 3-mL tetraethyl silicate (98 wt%) were added to the solution successively and the solution will continue to be stirred for 2 h at 180 r/min. Finally, $Y_2Fe_{17}N_{3-\delta}$@SiO_2 particles were successfully synthesized and collected after the washing and drying processes.

For obtaining the complex permeability and complex permittivity, $Y_2Fe_{17}N_{3-\delta}$/PU and $Y_2Fe_{17}N_{3-\delta}$@SiO_2/PU absorbers (YFN/PU and YFN@Si/PU) were prepared with different volume fractions (15 vol%, 20 vol%, 25 vol%, 30 vol%). Firstly, the polyurethane (PU) was completely dissolved in acetone under continuous ultrasonic condition. Then $Y_2Fe_{17}N_{3-\delta}$ or $Y_2Fe_{17}N_{3-\delta}$@SiO_2 particles were added and dispersed in the solution fully. Finally, the liquid composed of alloy particles, polyurethane and acetone was orientated in a parallel rotating magnetic field (1 T) for 15 minutes until acetone volatilized completely. After the above processes, the orientated composite was made into a toroidal shape sample ($\phi_{in} = 3.04$ mm, $\phi_{out} = 7.00$ mm) using a mold.

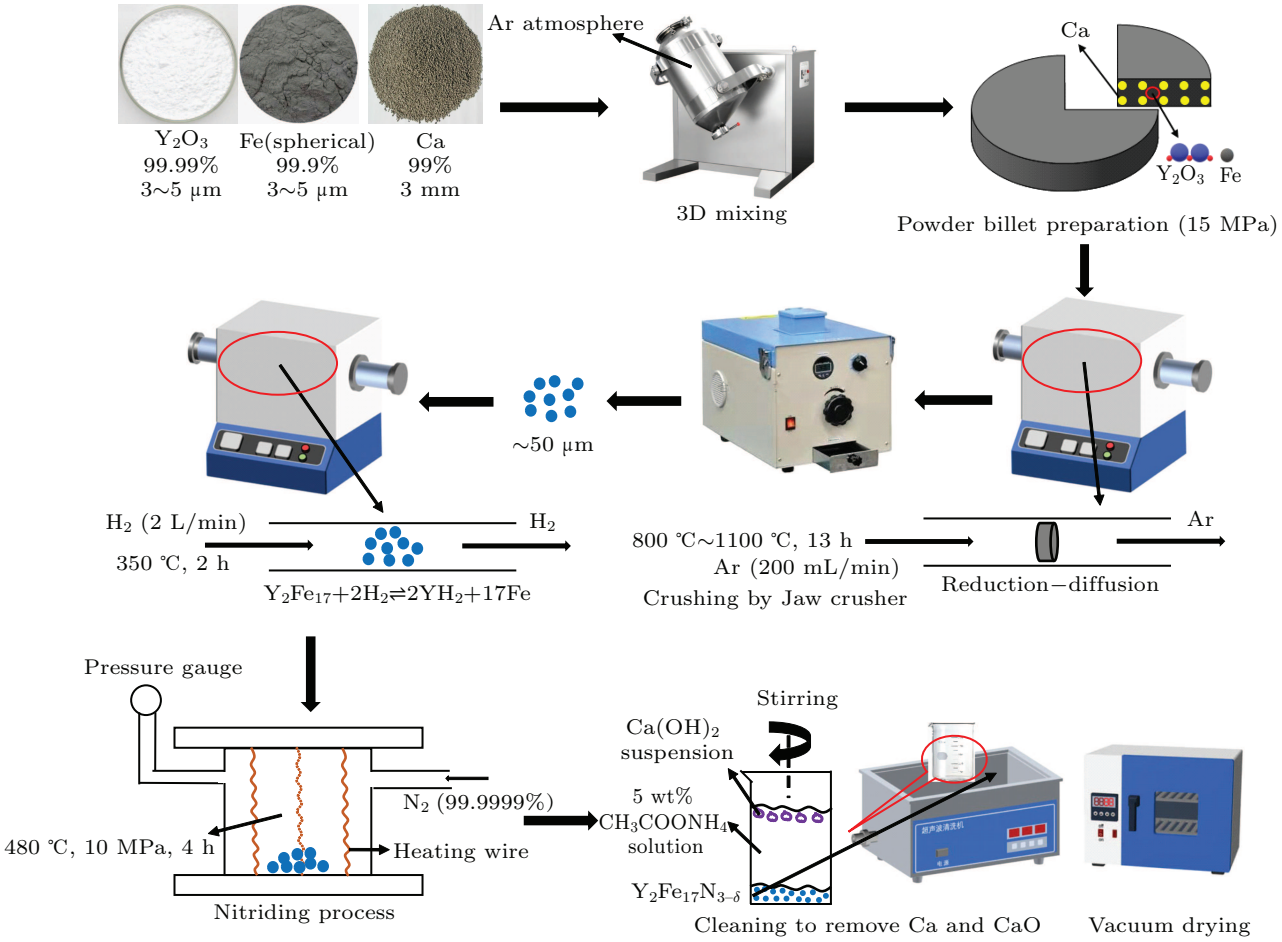


Fig. 1. The synthesis process of $Y_2Fe_{17}N_{3-\delta}$ particles.

2.3. Characterization

The crystal structures were characterized by x-ray diffraction (XRD, PANalytical X' Pert PRO). The elemental differences between different samples were analyzed by x-ray photoelectron spectroscopy (XPS, Kratos AXIS Ultra DLD). The morphology was analyzed by scanning electron microscope (SEM, Apreo S). The distribution of elements in samples was analyzed by the energy dispersive spectrometer (EDS, EDAX). The vibrating sample magnetometer (VSM, Microsence EV9) was used to measure the hysteresis loops of samples. The complex permeability and complex permittivity of absorbers were obtained using a vector network analyzer (Agilent Technologies N5247A) in the range of 0.1 GHz–18 GHz range.

3. Results and discussion

3.1. Characterization of structure, micromorphology, element, and magnetic properties

Figure 2(a) shows the XRD pattern of raw $Y_2Fe_{17}N_{3-\delta}$ particles. As shown in Fig. 2(a), the XRD pattern is completely consistent with PDF#86-0450 which is the standard card of $Y_2Fe_{17}N_{2.4}$. It is worth noting that the content of α-Fe precipitated from $Y_2Fe_{17}N_{3-\delta}$ is extremely low comparing with the previous work about $Re_2Fe_{17}N_{3-\delta}$ (Re = rare earth

elements).[2,10,19] This result shows that high pressure nitriding technology is a promising process for the preparation of pure $Re_2Fe_{17}N_{3-\delta}$. In Fig. 2(b), compared to $Y_2Fe_{17}N_{3-\delta}$ (broken) particles, the XRD pattern of $Y_2Fe_{17}N_{3-\delta}$@SiO_2 particles do not change significantly and the intensity of its diffraction peaks drop slightly. Therefore, the crystal structure of $Y_2Fe_{17}N_{3-\delta}$@SiO_2 particles has not been changed during the coating progress. As shown in Fig. 2(c), compared to $Y_2Fe_{17}N_{3-\delta}$ (broken) particles, the XPS of $Y_2Fe_{17}N_{3-\delta}$@SiO_2 particles have obvious intensity peaks at 100 eV and 551 eV respectively. These peaks and the XPS peaks of Si and O are at the same position which indicates that the $Y_2Fe_{17}N_{3-\delta}$@SiO_2 is composed of $Y_2Fe_{17}N_{3-\delta}$ and silica.

In Fig. 2(d), the loose, porous, and irregular structure and size ($\sim$ 50 μm) of raw $Y_2Fe_{17}N_{3-\delta}$ particles can be clearly and intuitively observed and the formation of this structure is due to the diffusion of Ca and the volatilization of Y during the synthesis process. The scanning electron microscopy (SEM) images exhibit the microscopic morphologies of $Y_2Fe_{17}N_{3-\delta}$ (broken) and $Y_2Fe_{17}N_{3-\delta}$@SiO_2 particles as displayed in Figs. 2(e) and 2(f). As shown in Fig. 2(e), the $Y_2Fe_{17}N_{3-\delta}$ (broken) particles display irregular shapes and the average size of $\sim$ 5 μm. In addition, as displayed in Fig. 2(f) and Fig. 3, $Y_2Fe_{17}N_{3-\delta}$@SiO_2 particles are covered tightly by nano-sized SiO_2 and agglomerated spherical silica attach to the surface of particles. In order to further characterize the distribution of elements after coating, the elemental mapping images of $Y_2Fe_{17}N_{3-\delta}$@SiO_2 particles are shown in Fig. 3. From the elemental mapping images, we can see that the element distribution is highly consistent with the shapes of $Y_2Fe_{17}N_{3-\delta}$@SiO_2 particles which indicates SiO_2 coats the surface of particles tightly and evenly.

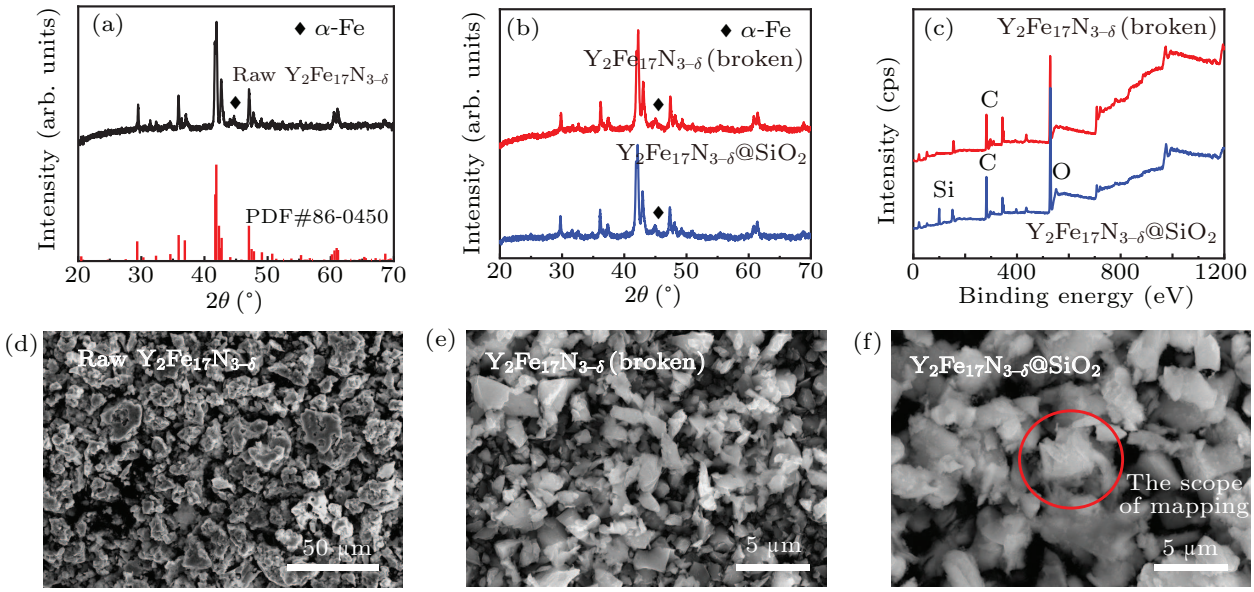


Fig. 2. (a) XRD pattern of raw $Y_2Fe_{17}N_{3-\delta}$ particles. (b) XRD patterns of $Y_2Fe_{17}N_{3-\delta}$ (broken) and $Y_2Fe_{17}N_{3-\delta}$@SiO_2 particles. (c) XPS of $Y_2Fe_{17}N_{3-\delta}$ (broken) and $Y_2Fe_{17}N_{3-\delta}$@SiO_2 particles. (d)–(f) SEM images of raw $Y_2Fe_{17}N_{3-\delta}$, $Y_2Fe_{17}N_{3-\delta}$ (broken), and $Y_2Fe_{17}N_{3-\delta}$@SiO_2 particles.

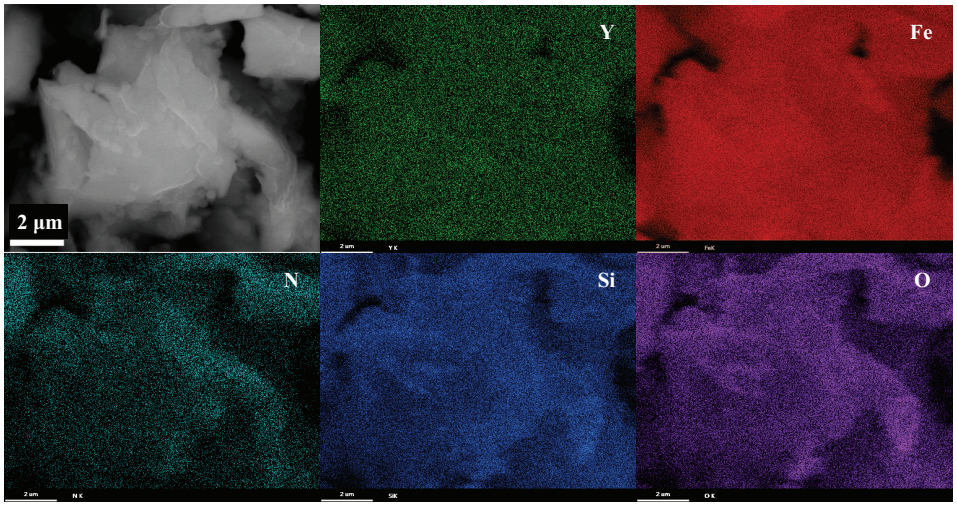


Fig. 3. The SEM image and elemental mapping images of $Y_2Fe_{17}N_{3-\delta}$@SiO_2 particles.

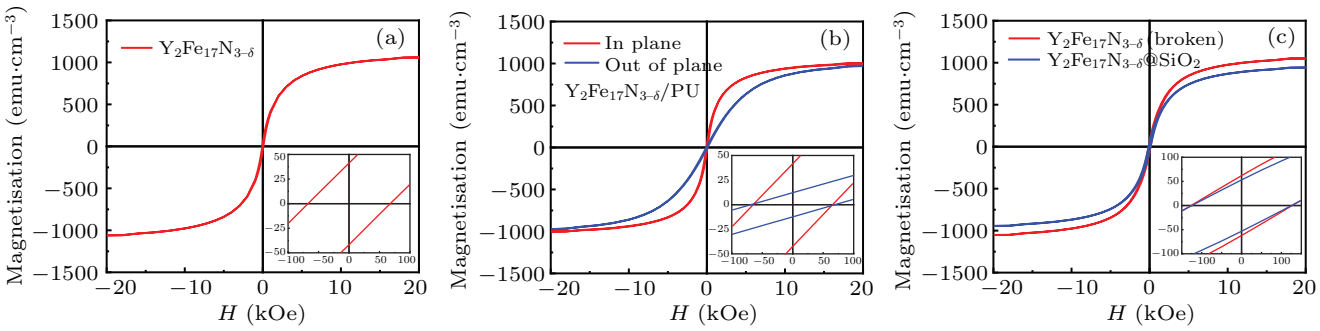


Fig. 4. (a) The hysteresis loop of raw $Y_2Fe_{17}N_{3-\delta}$ particles. (b) The hysteresis loops in-plane and out-of-plane directions of oriented $Y_2Fe_{17}N_{3-\delta}$/PU composite. (c) The hysteresis loops of $Y_2Fe_{17}N_{3-\delta}$ (broken) and $Y_2Fe_{17}N_{3-\delta}$@SiO_2 particles.

The hysteresis loop of raw $Y_2Fe_{17}N_{3-\delta}$ particles is shown in Fig. 4(a). As we can see, the coercivity (H_c) and the saturation magnetization (M_s) of raw $Y_2Fe_{17}N_{3-\delta}$ particles are 57.8 Oe (1 Oe = 79.5775 A·m^{-1}) and 1060.6 emu/cm^3 respectively. According to previous studies, the Curie temperature (T_C) is increased from 325 K to 694 K due to nitriding, which raised the microwave absorption application temperature of $Y_2Fe_{17}N_{3-\delta}$.[21,22] In the direction parallel and perpendicular to the plane of orientation, the hysteresis loops of oriented $Y_2Fe_{17}N_{3-\delta}$/PU composite are shown in Fig. 4(b). The expression of DPO is as follows:

$$\mathrm{DPO}\,(\%) = \frac{M_s - M_{r,\mathrm{out-of-plane}}}{M_s}, \tag{1}$$

where M_s is the saturation magnetization, $M_{r,\mathrm{out-of-plane}}$ is the remanence perpendicular to the plane of orientation. The oriented $Y_2Fe_{17}N_{3-\delta}$/PU composite has an excellent degree of plane orientation (DPO) 98.77% which further indicates that it is easy-plane microwave absorbing material.[11] Based on previous work about oriented microwave absorbers, the oriented composite absorber showed a dramatic increase in permeability and a remarkable decrease in the matching thickness.[13] In Fig. 4(c), the difference of hysteresis loops of $Y_2Fe_{17}N_{3-\delta}$ (broken) and $Y_2Fe_{17}N_{3-\delta}$@SiO_2 particles is shown. The M_s of $Y_2Fe_{17}N_{3-\delta}$@SiO_2 particles decreases from 1060.6 emu/cm^3 to 944.3 emu/cm^3 because SiO_2 cannot be magnetized and occupies a certain volume. In addition, compared to the raw $Y_2Fe_{17}N_{3-\delta}$ particles, the H_c of $Y_2Fe_{17}N_{3-\delta}$ and $Y_2Fe_{17}N_{3-\delta}$@SiO_2 particles increases from 57.8 Oe to 125.5 Oe because stress is generated in particles during ball milling process.

3.2. Impedance matching and microwave absorption properties of YFN/PU and YFN@Si/PU absorbers

The complex permeability ($\mu_r = \mu' - j\mu''$) and complex permittivity ($\varepsilon_r = \varepsilon' - j\varepsilon''$) of YFN/PU and YFN@Si/PU absorbers are measured by coaxial method at room temperature over 0.1 GHz–18 GHz and are shown in Fig. 5. Obviously, on the one hand, the values of complex permeability and permittivity are positively correlated with the volume fraction. On the other hand, under the same volume fraction, the complex permeability and complex permittivity of YFN@Si/PU absorbers decrease significantly relative to YFN/PU absorbers which is majorly due to the introduction of non-magnetic silica particles and the decrease of electrical conductivity after silica coating. In addition, comparing with YFN/PU absorbers, the resonance peaks of YFN@Si/PU absorbers still in relaxation mode do not change significantly.

The previous work on microwave absorption shows that the excellent property of absorber depends on two key factors which are phase matching and amplitude matching respectively. On the one hand, according to interfacial reflection model, the thickness and applied frequency of absorber must satisfy the theory of $\lambda/4$ interference cancellation for phase matching (phase difference $= \pi$).[2,23] The schematic diagram of interfacial reflection model and $\lambda/4$ interference cancelation theory is shown in Fig. 6. On the other hand, according to the matching theory in free space, the amplitudes of reflection waves are equal ($|\Gamma| = |\Pi|$) when impedance matching $|Z_{in}/Z_0| = 1$.[2,24,25] Therefore, the strongest reflection loss (RL_{min}) can be obtained if the above two conditions are satisfied (perfect matching).

According to interface reflection model, $\lambda/4$ interference cancellation theory and transmission line theory, matching thickness (t_m), input impedance (Z_{in}), and the reflection loss (RL) of absorbers are calculated in the following equations:[13]

$$t_m = \frac{nc}{4f_m\sqrt{|\mu_r\varepsilon_r|}}, \quad (n = 1,3,5,\ldots), \tag{2}$$

$$Z_{in} = Z_0\sqrt{\mu_r/\varepsilon_r}\tanh\left(j\frac{2\pi ft}{c}\sqrt{\mu_r\varepsilon_r}\right), \tag{3}$$

$$\mathrm{RL}\,(\mathrm{dB}) = 20\log\left|\frac{Z_{in} - Z_0}{Z_{in} + Z_0}\right|, \tag{4}$$

in which f is the application frequency, c is the velocity of light in free space, t is the thickness of absorber, and Z_0 is the impedance of air.

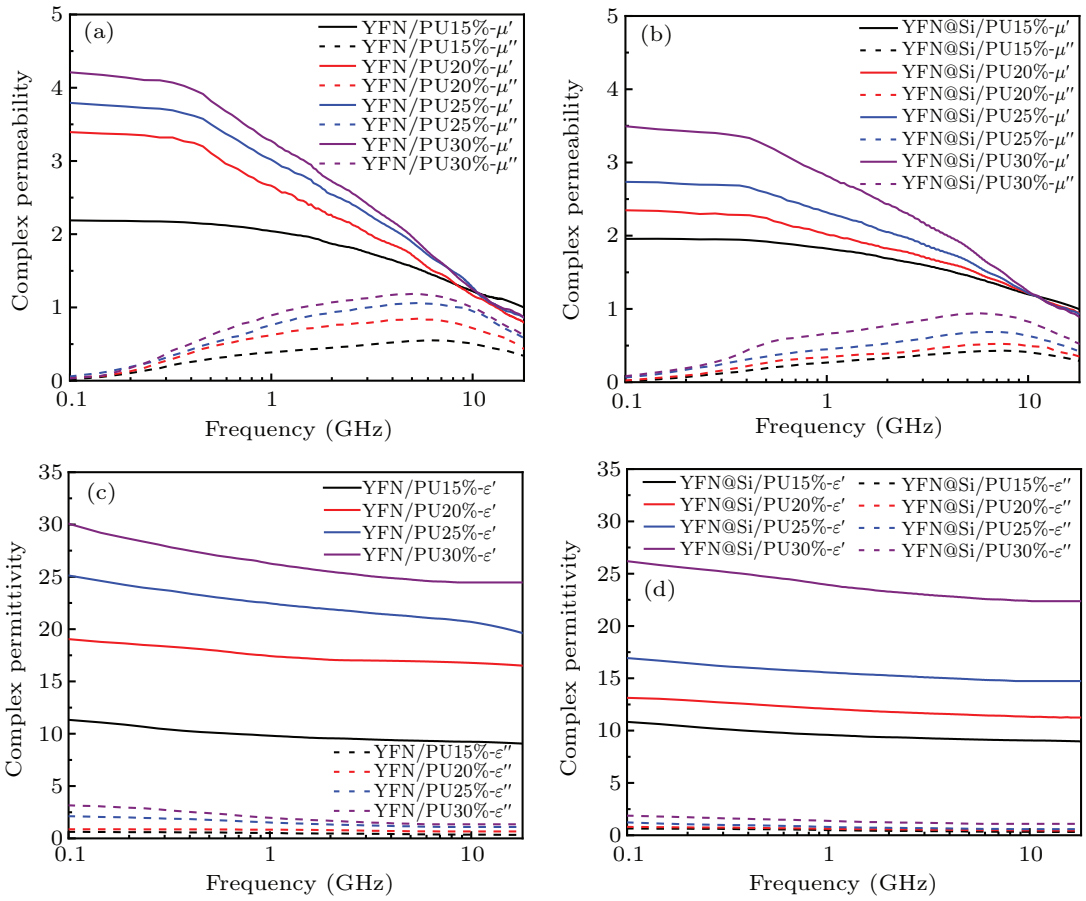


Fig. 5. (a)–(b) Complex permeability, (c)–(d) complex permittivity of YFN/PU and YFN@Si/PU absorbers depended on frequency under different volume fractions.

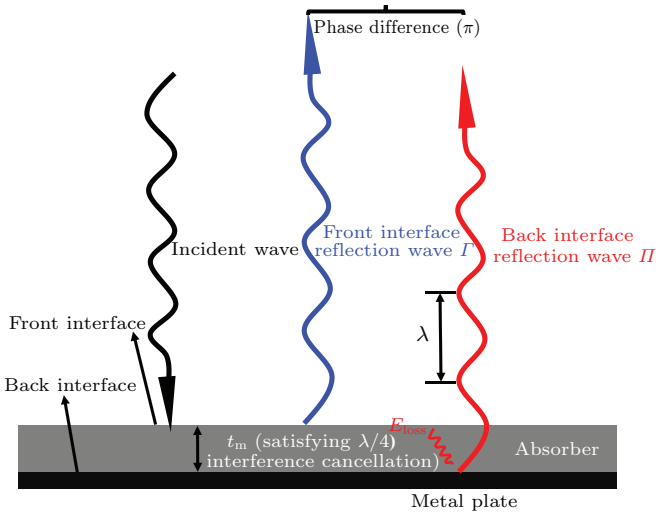


Fig. 6. Schematic diagram of interface reflection model and $\lambda/4$ interference cancellation theory.

For YFN/PU and YFN@Si/PU absorbers, according to Eqs. (2), (3), and (4), we can obtain impedance matching ($|Z_{in}/Z_0|$), matching thickness (t_m, $n = 1$) and the strongest reflection loss depended on frequency as shown in Fig. 7. As shown in Figs. 7(a) and 7(b), as the volume fraction increases, the best impedance matching frequency point ($|Z_{in}/Z_0| = 1$) moves to the low frequency. At the same volume fraction, the best impedance matching frequency points of YFN@Si/PU absorbers are at higher frequencies. In addition, the best impedance matching frequency point of YFN@Si/PU absorber varies more regularly with the volume fraction, which is helpful to determine the best volume fraction of the absorber at a certain applied frequency. We also observed that too low volume fraction (15 vol%) cannot achieve the best impedance matching because the value of $|Z_{in}/Z_0|$ is always larger than 1.

Before and after coating, the change of matching thickness (t_m) with frequency is shown in Figs. 7(c) and 7(d). Since coating reduces complex permeability and permittivity, the t_m of YFN@Si/PU absorber increases slightly at the same frequency and volume fraction. However, owing to the increase of best matching frequency, the thicknesses of perfect matching of YFN@Si/PU absorbers greatly decrease eventually. Therefore, silicon dioxide coating is beneficial to reduce the matching thickness and realize the light weight of the absorber. Finally, combined with Figs. 7(a), 7(c), 7(e) or 7(b), 7(d), 7(f), we can obtain the perfect matching thicknesses and the strongest reflection loss of YFN@/PU and YFN@Si/PU absorbers under different volume fractions.

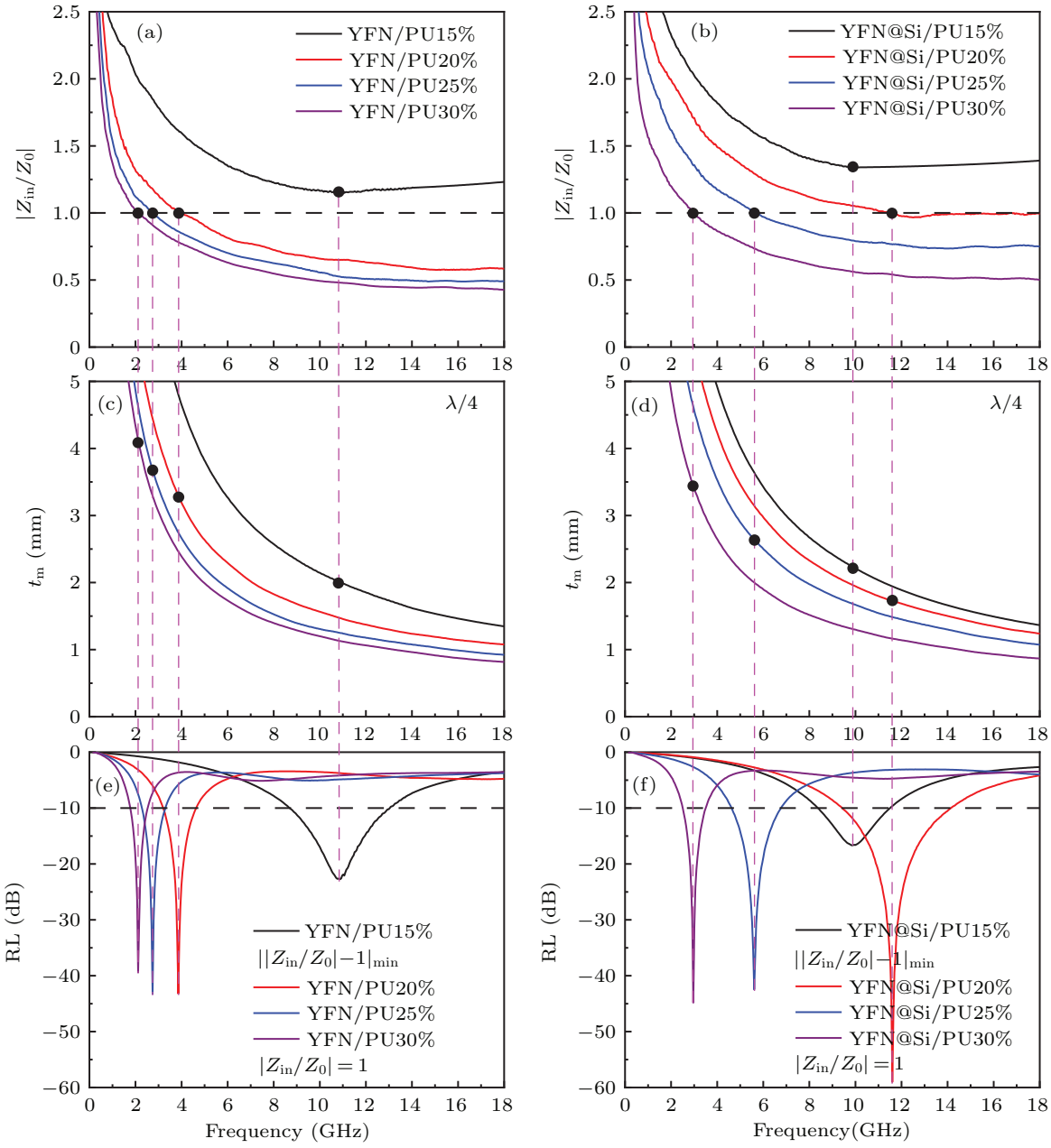


Fig. 7. (a)–(b) Impedance matching ($|Z_{in}/Z_0|$), (c)–(d) matching thickness (t_m, $n = 1$), and (e), (f) the strongest reflection loss of YFN/PU and YFN@Si/PU absorbers depended on frequency under different volume fractions.

In practical application, it is meaningless to discuss only the value of reflection loss peak without considering the matching thickness, microwave absorption bandwidth, and applied frequency band. Therefore, in order to show the microwave absorption properties vividly, the RL of absorbers depended on thickness and frequency under different volume fractions is shown in the form of contour figures (color fill) as shown in Fig. 8. The contour lines of −10 dB and −20 dB are labeled which indicate that microwave energy absorption efficiencies of absorber are 90% and 99% respectively.

There are several starting points of the characterization of absorber's property. From the point of perfect matching, the RL_{min} and EAB of YFN/PU (20 vol%) absorber is −43.23 dB and 1.43 GHz respectively at 3.86 GHz with thickness of 3.29 mm; In contrast, the RL_{min} value and EAB of YFN@Si/PU (20 vol%) absorber is −59.02 dB and 4.74 GHz respectively at 11.60 GHz with thickness of 1.70 mm. The above data shows that YFN@Si/PU absorbers are more conducive to the realization of microwave absorption material standards which are thin thickness, light weight, strong absorbing intensity, and broad bandwidth. From the point of EAB covering given frequency bands, in order to illustrate the microwave absorption properties of absorbers in X-band (8 GHz–12 GHz) and Ku-band (12 GHz–18 GHz), the related parameters are shown in Figs. 8(c), 8(d), 8(f), and Table 2. Therefore, it is necessary to choose between RL and the coverage frequency band of EAB in absorber's design.

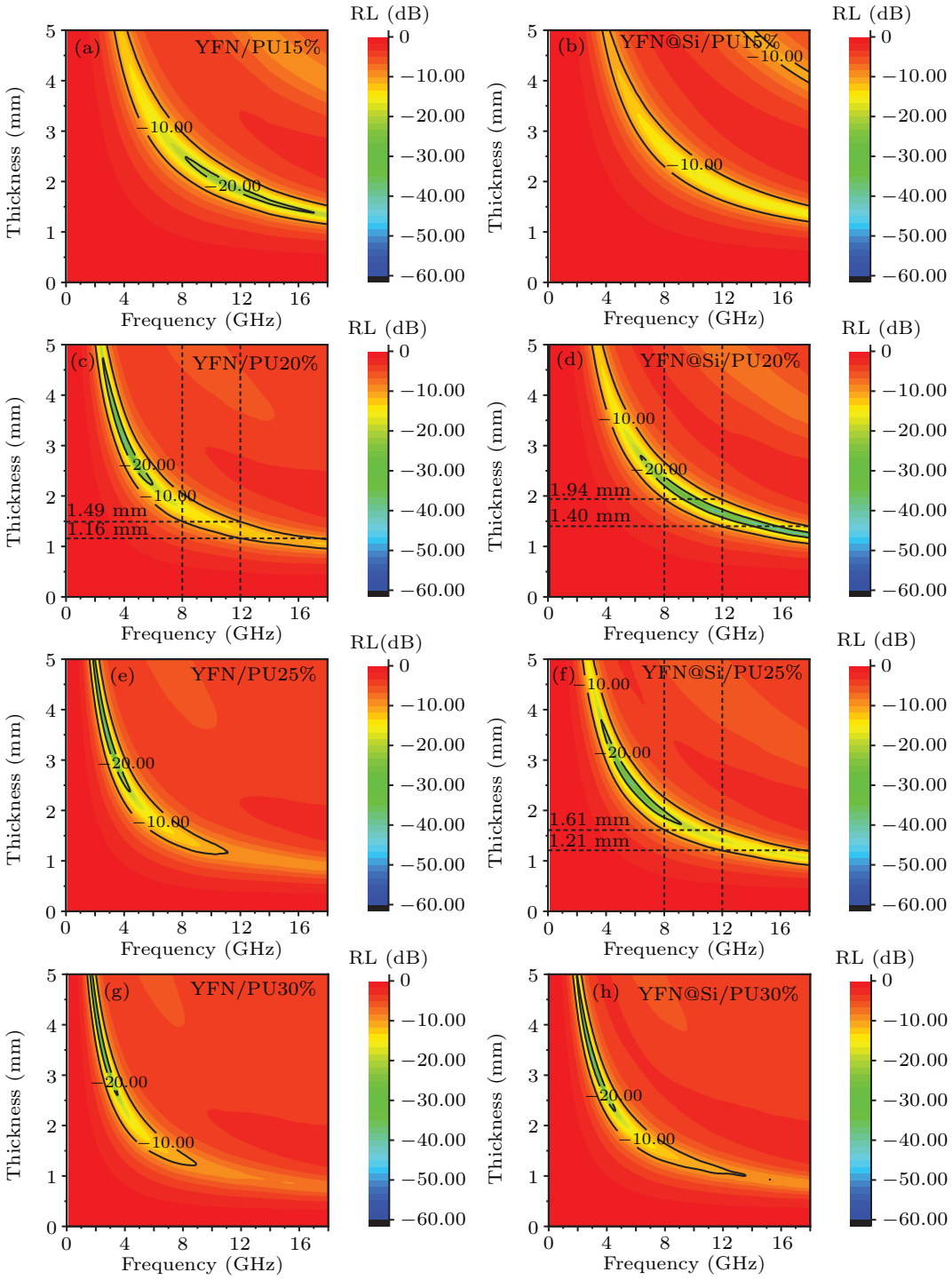


Fig. 8. The reflection loss of YFN/PU and YFN@Si/PU absorbers depended on thickness and frequency under different volume fractions.

Table 2. The parameters related to microwave absorption properties of YFN/PU (20 vol%) and YFN@Si/PU (20 vol%, 25 vol%) absorbers.

Sample	Volume fraction (%)	Thickness (mm)	f_m (GHz)	EAB (GHz)	RL_{min} (dB)
YFN/PU	20	3.29	3.86	1.43	43.23
		1.49	9.86	X-band	13.78
		1.16	14.02	Ku-band	11.66
YFN@Si/PU	20	1.70	11.60	4.74	59.02
		1.94	9.81	X-band	30.91
		1.40	14.96	Ku-band	50.01
YFN@Si/PU	25	2.64	5.60	2.15	42.46
		1.61	9.95	X-band	18.69
		1.21	14.87	Ku-band	16.87

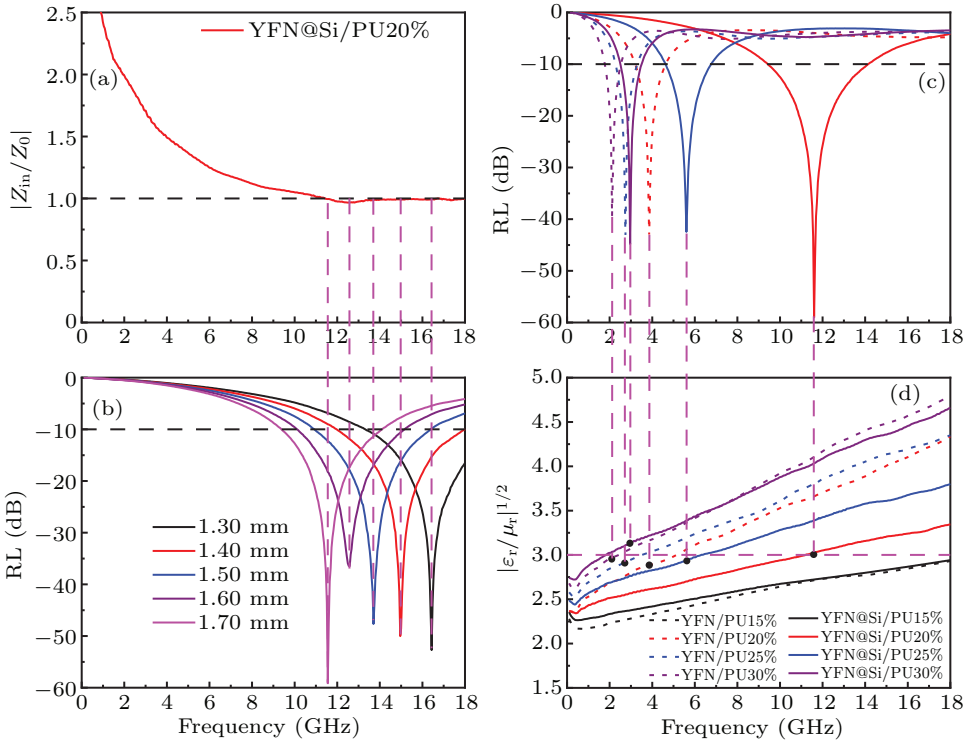


Fig. 9. (a) The $|Z_{in}/Z_0|$–f curve and (b) RL of YFN@Si/PU (20 vol%) absorber vary between 11.60 GHz–18 GHz at different thicknesses. (c) The RL_{min} and (d) reflection factor ($\sqrt{\varepsilon_r/\mu_r}$) of YFN/PU and YFN@Si/PU absorbers depended on frequency under different volume fractions.

In this experiment, YFN@Si/PU (20 vol%) absorber is always in the almost best impedance matching state within the range of 11.60 GHz–18 GHz as shown in Figs. 9(a) and 9(b). In this case, we can change the frequency range of microwave absorption by just adjusting the thickness with little effect on the RL_{min} and EAB. Therefore, as a key parameter, the volume fraction under this case should be concerned and referenced in the design of absorber. The reflection factor ($\sqrt{\varepsilon_r/\mu_r}$) is observed to be closely related to the perfect impedance matching of absorber.[5] For an electromagnetic wave normally incident to an absorber layer, the amplitudes of front and back interface reflection waves can be expressed as[26] (Suppose the amplitude of the incident wave is 1)

$$\Gamma = \left(\sqrt{\mu_r/\varepsilon_r} - 1\right) / \left(\sqrt{\mu_r/\varepsilon_r} + 1\right), \tag{5}$$

$$\Pi = \left(\Gamma^2 - 1\right) T^2 / \left(1 - \Gamma T^2\right). \tag{6}$$

The factor $T = \exp\left[\mathrm{j}\left(2\pi f t/c\right)\sqrt{\mu_r\varepsilon_r}\right]$ takes into account the attenuation of the wave in the absorber layer. When absorber is in the perfect matching, $|Z_{in}/Z_0| = 1$, $|\Gamma| = |\Pi|$. According to Eqs. (3), (5), and (6), we can calculate that $\sqrt{\varepsilon_r/\mu_r}$ is equal to 3. Figures 9(c) and 9(d) show the direct correlation between perfect matching point (RL_{min}) and $\sqrt{\varepsilon_r/\mu_r}$ under different volume fractions. The values of $\sqrt{\varepsilon_r/\mu_r}$ corresponding to the RL_{min} are always around 3 which agrees well with the theoretical value 3.

3.3. Influencing factors and bandwidth formula of effective absorption bandwidth (EAB: RL < -10 dB)

In the previous work, as the main parameter of microwave absorption property, effective absorption bandwidth has been concerned and studied. As the RL peak comes from the cancelation of the front interface reflection wave (Γ) and back interface reflection wave (Π), their phase difference should be π at the peak frequency point. When the frequency deviates from the peak frequency point by Δf, the peak intensity will decrease due to that the phase difference of the two reflected waves deviates from π to $\pi - \theta$ or $\pi + \theta$.[23,27] Figure 10 is a schematic analysis of the microwave absorption bandwidth based on the origin of bandwidth and mathematical model. As shown in Figs. 10(a), 10(c), and 10(d), Δf is the half bandwidth at -10 dB, RL_1 is the reflection loss at a specified point, RL_0 is the reflection loss at the peak frequency point, A is the amplitude of the reflection wave ($A = |\Gamma + \Pi|$). Starting from microwave amplitude, the derivation process of effective bandwidth formula is shown as follows taking YFN@Si/PU (25 vol%) absorber for example.

As shown in Figs. 10(a) and 10(b), when the reflection losses are RL_0 and RL_1 respectively, the amplitudes of reflection wave are A_0 and A_1 respectively which can be written as

$$A_0 = \Gamma\cos 0 + \Pi\cos\pi = \Gamma - \Pi, \tag{7}$$

$$A_1 = \Gamma\cos 0 + \Pi\cos\left(\pi \pm \theta\right) = \Gamma - \Pi\cos\theta. \tag{8}$$

Hence, the difference between A_1 and A_0 can be written as

$$A_1 - A_0 = \Pi\left(1 - \cos\theta\right). \tag{9}$$

Assuming that θ is small enough, it can be described by Taylor expansion recursion formula

$$1-\cos\theta \approx \frac{\theta^2}{2!} = \frac{\theta^2}{2}. \tag{10}$$

According to Eqs. (9) and (10), we can get

$$\theta = \left(\frac{2(A_1 - A_0)}{\Pi}\right)^{1/2}. \tag{11}$$

According to the origin of bandwidth and mathematical model which are shown in Figs. 10(a) and 10(b), the relationship between θ and Δf is described as

$$\frac{\theta}{\pi} = \frac{\left|\frac{\mathrm{d}t_\mathrm{m}}{\mathrm{d}f}\right| \cdot 2\Delta f}{t_\mathrm{m}}. \tag{12}$$

The formula of EAB is obtained as

$$\Delta = 2\Delta f = \frac{\theta t_\mathrm{m}}{\pi |\mathrm{d}t_\mathrm{m}/\mathrm{d}f|} = \frac{t_\mathrm{m}}{\pi |\mathrm{d}t_\mathrm{m}/\mathrm{d}f|}\left(\frac{2(A_1 - A_0)}{\Pi}\right)^{1/2}. \tag{13}$$

When absorber is in perfect matching and enough complex permeability and permittivity data points are measured, $\mathrm{RL}_0 = -\infty$, $A_1 = 10^{-(10/20)} = 0.3162$, $A_0 = 10^{(-\infty/20)} \approx 0$. Finally, the formula of EAB can be expressed by

$$\Delta = \frac{t_\mathrm{m}\sqrt{0.6325/\Pi}}{\pi |\mathrm{d}t_\mathrm{m}/\mathrm{d}f|}.$$

Equation (13) demonstrates that EAB is mostly influenced by the thickness, the derivation of matching thickness to frequency and the amplitude of the front interface reflection wave. In the above factors, bandwidth is most sensitive to the $|\mathrm{d}t_\mathrm{m}/\mathrm{d}f|$. According to Eq. (13), the related parameters of the calculated and experimental bandwidth are listed under various thicknesses as shown in Table 3. Obviously, the bandwidths from the theoretical calculations under various thicknesses agree well with those of the experimental results.

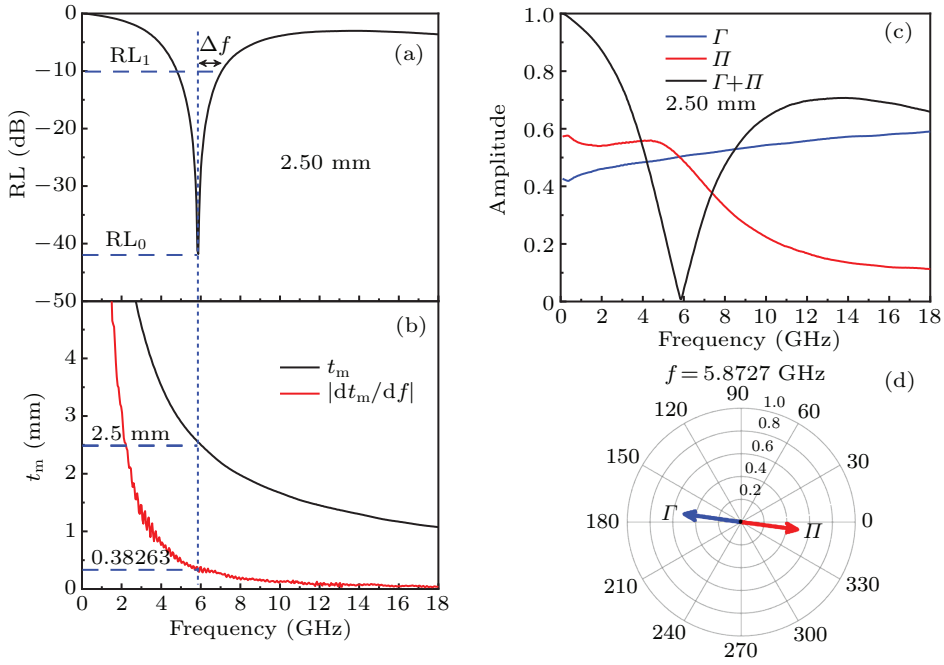


Fig. 10. (a) The RL–f, (b) t_m–f and $|\mathrm{d}t_\mathrm{m}/\mathrm{d}f|$–$f$ curves. (c) Γ, Π, and $\Gamma+\Pi$ vary with frequency. (d) The vector pole figure of Γ and Π at 5.8726 GHz for YFN@Si/PU (25 vol%) absorber with thickness of 2.50 mm.

Table 3. The parameters of the calculated and experimental bandwidth (RL < -10 dB) for YFN@Si/PU (25 vol%) absorber under various thicknesses.

t (mm)	f_m (GHz)	$\lvert\mathrm{d}t_\mathrm{m}/\mathrm{d}f\rvert$	RL_0 (dB)	Π	$\Delta_\mathrm{calculated}$ (GHz)	$\Delta_\mathrm{experimental}$ (GHz)
1.50	11.47	0.10971	–18.26	0.4279	3.95	4.56
2.00	7.89	0.18681	–24.28	0.4590	3.78	3.13
2.50	5.87	0.38263	–41.80	0.4965	2.58	2.28
3.00	4.80	0.56246	–26.22	0.5350	1.70	1.75
3.50	4.04	0.80902	–21.84	0.5755	1.13	1.30

4. Conclusion

In summary, $Y_2Fe_{17}N_{3-\delta}$@SiO_2 particles were synthesized by reduction diffusion, high pressure nitriding, and silica coating method. The structure, morphology, element and magnetic properties of $Y_2Fe_{17}N_{3-\delta}$ and $Y_2Fe_{17}N_{3-\delta}$@SiO_2 particles were characterized. The complex permittivity and complex permeability of YFN/PU and YFN@Si/PU absorbers were characterized over 0.1 GHz–18 GHz. By being coated with silica, the impedance matching and microwave absorption properties of YFN@Si/PU absorbers were regulated and

compared with those of YFN/PU absorbers. The result indicates that YFN@Si/PU absorbers are more conducive to the realization of microwave absorption material standards which are thin thickness, light weight, strong absorbing intensity, and broad bandwidth. The microwave absorption properties of absorbers are characterized from the practical applied frequency bands (X-band and Ku-band). In addition, the reflection factor ($\sqrt{\varepsilon_r/\mu_r}$) is closely related to the perfect impedance matching of absorber and the experimental values agree well with the theoretical value 3. Finally, the formula of effective absorption bandwidth is derived and simplified from the origin of bandwidth and mathematical model. The bandwidths from the theoretical calculations under various thicknesses are almost in accordance with those of the experimental results.

Acknowledgements

Project supported by the National Key Research and Development Program of China (Grant No. 2021YFB3501300), the National Natural Science Foundation of China (Grant No. 51731001), and the Fund from the State Key Laboratory of Baiyunobo Rare Earth Resource Researches and Comprehensive Utilization's Key Research and Development Projects.

References

[1] Wang B L, Wu Q, Fu Y G and Liu T 2021 *J. Mater. Sci. Technol.* **86** 91
[2] Zhuang X H, Tan G G, Ning M Q, Qi C Y, Ge X J, Yang Z and Man Q K 2021 *J. Alloys Compd.* **883** 160835
[3] Fan Y, Wang J Y, Zhang X M, Zhu Z S, Liu Y, Xie A T, Bai H C and Kong L B 2021 *Diam. Relat. Mater.* **120** 108685
[4] Qin G Y, Huang X X, Yan X, He Y F, Liu Y H, Xia L and Zhong B 2022 *J. Adv. Ceram.* **11** 105
[5] Wang T, Zhang J M, Wang P, Qiao L, Tang L Y, Xue D S and Li F S 2016 *J. Magn. Mater. Dev.* **47** No. 6 (in Chinese)
[6] Li X, Huang C, Wang Z L, Xiang Z and Lu W 2021 *J. Alloys Compd.* **879** 160465
[7] Ling A, Pan J, Tan G G, Gu X S, Lou Y X, Chen S W, Man Q K, Li R W and Liu X C 2019 *J. Alloys Compd.* **787** 1097
[8] Xiang Z, Zhang X, Shi Y Y, Cai L, Cheng J, Jiang H J, Zhu X J, Dong Y Y and Lu W 2021 *Carbon* **185** 477
[9] Zhu X J, Dong Y Y, Pan F, Xiang Z, Liu Z C, Deng B W, Zhang X, Shi Z and Lu W 2021 *Compos. Commun.* **25** 100731
[10] Tan G G, Zhang Y B, Qiao L, Wang T, Wang J B and Li F S 2015 *Physica B* **477** 52
[11] Wu P, Zhang Y D, Hao H B, Qiao L, Liu X, Wang T and Li F S 2022 *J. Magn. Magn. Mater.* **549** 168962
[12] Wang P, Zhang J M, Wang G W, Duan B F, Wang T and Li F S 2020 *Appl. Phys. Lett.* **116** 112403
[13] Zuo W L, Qiao L, Chi X, Wang T and Li F S 2011 *J. Alloys Compd.* **509** 6359
[14] He Y, Pan S K, Cheng L C, Luo J L and Yu J J 2019 *J. Electron. Mater.* **48** 1574
[15] Qiao G Y, Yang W Y, Lai Y F, Tian G, Zha L, Hu Q W, Liu S Q, Wang C S, Han J Z, Du H L, Yang Y C and Yang J B 2019 *Mater. Res. Express* **6** 016103
[16] Xiong J L, Pan S K, Cheng L C, Lin P H, Yao Q R and Fan Y L 2017 *Rare Metal Mater. Eng.* **46** 2060
[17] Gu X S, Tan G G, Chen S W, Man Q K, Chen S L, Jiang L Q, Chang C T, Wang X M, Li F S and Li R W 2017 *Mater. Sci. Forum* **898** 1638
[18] He Y, Pan S K, Cheng L C, Luo J L, Xu Y Q, Yu J J and Chang J Q 2018 *J. Mater. Sci. Mater. Electron.* **29** 12624
[19] Hu Q W, Qiao G Y, Yang W Y, Liu Z, Zhang P Y, Liu S Q, Wang C S, Zhou D, Han R, Cai D Y, Hu B Q and Yang J B 2020 *J. Phys. D* **53** 115001
[20] Zhou Y Y, Xie H, Zhou W C and Ren Z W 2018 *J. Magn. Magn. Mater.* **446** 143
[21] Qtani Y, Hurley D P F, Sun H and Coey J M D 1991 *J. Appl. Phys.* **69** 5584
[22] Sun H, Coey J M, Otani Y and Hurley D P F 1990 *J. Phys.: Condens. Matter* **2** 6465
[23] Wang T, Han R, Tan G G, Wei J J, Qiao L and Li F S 2012 *J. Appl. Phys.* **112** 104903
[24] Wang X, Pan F, Xiang Z, Zeng Q W, Pei K, Che R C and Lu W 2020 *Carbon* **157** 130
[25] Naito Y and Suetake K 1971 *IEEE Trans. Microw. Theory Tech.* **19** 65
[26] Qiao L, Wang T, Mei Z L, Li X L, Sui W B, Tang L Y and Li F S 2016 *Chin. Phys. Lett.* **33** 027502
[27] Wang T, Wei J J, Zhang Z Q and Li F S 2013 *Mater. China* **32** No. 2